

Numerical Simulation of Ice Crystal Impact, Adhesion and Icing of Multi-element Airfoil Under Mixed-Phase Icing Conditions

LIU Zonghui¹, BU Xueqin^{1*}, HUANG Ping¹, LIN Guiping^{2,1}, WANG Yudong¹

1. School of Aeronautic Science and Engineering, Beihang University, Beijing 100083, P. R. China;

2. Hangzhou Innovation Institute, Beihang University, Hangzhou 311115, P. R. China

(Received 24 Marth 2023; revised 24 December 2023; accepted 15 March 2024)

Abstract: The investigation of aircraft icing problems has led to a growing interest in mixed-phase icing. This paper used drag coefficient, adhesion, and icing thermodynamic models to calculate ice accretion on a quasi-three-dimensional multi-element airfoil under mixed-phase conditions. Firstly, mesh generation and airflow field calculations are conducted on the multi-element airfoil. Next, numerical simulations are carried out to analyze the characteristics of ice crystals impingement, adhesion, and ice accretion under mixed phase conditions. The results show that the adhesion mass flow rate of ice crystals is high and can pose a threat to flight safety, and adhesion may also occur in the runback water zone. Moreover, with the increase of liquid water content (LWC) over total water content (TWC), ice crystals are more likely to adhere to surfaces and participate in surface icing.

Key words: multi-element airfoil; mixed-phase icing; impact model; adhesion model; icing thermodynamic model

CLC number: V244.1

Document code: A

Article ID: 1005-1120(2024)02-0202-16

0 Introduction

Since the beginning of modern aircraft flight, the problem of aircraft icing has received increasing attention. From the perspective of icing causes, aircraft icing can be divided into supercooled water icing and ice crystal icing, where ice crystal icing can be divided into glaciated icing conditions and mixed-phase icing conditions. Mixed-phase icing conditions are complex meteorological conditions where both supercooled water droplets and ice crystals exist. Early aircraft icing studies focused on supercooled water droplets icing, but in recent years, aircraft icing studies have gradually expanded from supercooled water droplets icing to ice crystals icing^[1-3]. Mason et al.^[4] concluded that turbofan engine power loss is closely related to ice crystal icing.

The hazards and mechanisms of icing caused by supercooled water droplets have been intensively

studied. However, the mechanism of ice crystal icing remains unclear, and it is generally believed that ice crystal icing requires the presence of liquid water^[5]. In glaciated conditions, the ice crystals will not adhere when they hit the cold airfoil, tailplane, and other cold surfaces as they will bounce off. When ice crystals hit hot surfaces or move in warm environment such as core of the engine, they will melt into liquid water. The presence of liquid water can cause ice crystals to adhere and eventually melt, which in turn absorbs heat as it melts, reducing the temperature of the hot surface and the surrounding environment. Severe ice crystal icing that occurs in the internal core parts of the engine may cause loss of engine power, surge, stalling, etc. Ice shedding may cause mechanical damage to the engine. In mixed-phase conditions, with the presence of liquid water, icing can form on the cold airfoil, tailplane, fin, and other cold surfaces. This can result in dam-

*Corresponding author, E-mail address: buxueqin@buaa.edu.cn.

How to cite this article: LIU Zonghui, BU Xueqin, HUANG Ping, et al. Numerical simulation of ice crystal impact, adhesion and icing of multi-element airfoil under mixed-phase icing conditions[J]. Transactions of Nanjing University of Aeronautics and Astronautics, 2024, 41(2):202-217.

<http://dx.doi.org/10.16356/j.1005-1120.2024.02.006>

age to the aerodynamic configuration of the aircraft, leading to a reduction in lift and an increase in drag, which can threaten flight safety. Icing can also occur on sensors, engine blades, and other hot surfaces, leading to abnormal sensor operation and posing a risk to the engine. Ice crystals play an important role in icing events that occur under mixed phase conditions.

Experimental studies of ice crystal icing require the support of advanced icing wind tunnels and expertise in various methodologies such as ice crystal preparation, transportation, and recreation of realistic icing-related meteorological scenarios^[6-8]. Conducting experiments can be a costly and technically challenging endeavor. Therefore, numerical simulations have become an essential tool for ice crystal icing due to their time and labor saving advantages. Manuel et al.^[9] used a potential flow code to analyze the motion of ice crystals within the turbofan engine core. The simulation analysis has been conducted in GleenICE using the E3 model of Wright et al^[10]. Habashi and Nored et al.^[11-13] explored the phase transition properties of ice crystal motion using Eulerian and Lagrangian methods.

There are relatively few domestic studies on aircraft icing in mixed-phase conditions. Zhang et al.^[14] used the FLUENT software to study the mixed-phase icing problem. Yuan et al.^[15] conducted a comprehensive review of the research on the phenomenon of ice crystal accretion in jet engines. They also highlighted the distinctions between ice crystal icing and supercooled water icing, and the test procedures and calculation methods of ice crystal icing. Jiang et al.^[16] calculated and analyzed the heat and mass transfer of ice crystals during their movement in the internal channel of turbofan engine, and obtained the impact characteristics of ice crystals inside the engine. Bu et al.^[17], based on the NACA 0012 airfoil, established an icing thermodynamic model for mixed-phase icing conditions and compared the calculation results with wind tunnel experiments. Based on the Lagrangian method, Ma et al.^[18] systematically analyzed the influence law of different parameters on ice crystal adhesion, which laid the foundation for further progress in the numer-

ical simulation of mixed-phase icing.

This paper combines the irregular particle drag model, ice crystal adhesion model and icing thermodynamic model to calculate the impingement, adhesion characteristics, and icing on a quasi-three-dimensional multi-element airfoil under mixed-phase conditions. The Eulerian method is used to calculate the motion of water droplets and ice crystals. The adhesion model and the icing thermodynamic model are applied and validated. Ice crystal icing on a quasi-three-element airfoil under mixed-phase conditions is simulated and analyzed. The simulation model and method in this paper provide support for ice crystal accretion calculations under mixed-phase conditions.

1 Calculation Models

1.1 Airflow field and particle motion model

The airflow field is calculated before the calculation of the impingement characteristics of particles (water droplets and ice crystals). Reynolds-averaged Navier-Stokes equations (RANS) are utilized to describe the airflow field, closing the RANS equations using the Spalart-Allmaras turbulence model. The RANS equations are presented as follows

$$\frac{\partial \rho_a}{\partial t} + \frac{\partial(\rho_a u_i)}{x_i} = 0 \tag{1}$$

$$\begin{aligned} \frac{\partial}{\partial t}(\rho_a u_i) + \frac{\partial}{\partial x_j}(\rho_a u_i u_j) = & -\frac{\partial p}{\partial x_i} + \\ \frac{\partial}{\partial x_j} \left[\mu \left(\frac{\partial u_i}{\partial x_j} + \frac{\partial u_j}{\partial x_i} - \frac{2}{3} \delta_{i,j} \frac{\partial u_1}{\partial x_1} \right) \right] + & \frac{\partial}{\partial x_j} (-\rho_a \overline{u'_i u'_j}) \end{aligned} \tag{2}$$

where ρ_a is the air density, u the Reynolds average velocity vector, p the pressure, and μ the dynamic viscosity. The subscripts i and j are the components in the x and y directions, respectively. The Reynolds stress term $-\rho_a \overline{u'_i u'_j}$ is defined by the Boussinesq assumption as

$$-\rho_a \overline{u'_i u'_j} = -p_t \delta_{i,j} + \mu_t \left(\frac{\partial u_i}{\partial x_j} + \frac{\partial u_j}{\partial x_i} \right) - \frac{2}{3} \mu_t \frac{\partial u_1}{\partial x_1} \delta_{i,j} \tag{3}$$

where $\delta_{i,j}$ is the Kronecker tensor component, μ_t the

turbulent viscosity, and k the turbulent energy. u'_i and u'_j are the pulse velocity components.

The motion of water droplets and ice crystals belongs to the two-phase flow between air and particles. The basic assumptions are as follows: (1) The content of water droplets and ice crystals in the air is very small (less than 1.87 g/m^3). The effect of air on particles is considered, and the effect of particles on the airflow is neglected. The coupling between air and particles is one-way. (2) Only the air drag of the particles is considered. The gravity and buoyancy forces are ignored. (3) The deformation, evaporation, sublimation or collisional fusion of particles are not considered during particle motion. The equivalent diameter of the particle is assumed to be constant. (4) The heat transfer between the particle and the surrounding air is ignored and the physical parameters of the particle remain constant. (5) The initial velocity of the particles is the same as the surrounding air.

Based on the above assumptions, the continuity and momentum equations of the particle flow field are expressed as

$$\frac{\partial(\rho\alpha)}{\partial t} + \nabla \cdot (\rho\alpha\mathbf{u}) = 0 \quad (4)$$

$$\frac{\partial(\rho\alpha\mathbf{u})}{\partial t} + \nabla \cdot (\rho\alpha\mathbf{u}\mathbf{u}) = \rho\alpha K(\mathbf{u}_a - \mathbf{u}) + \rho\alpha\mathbf{F} \quad (5)$$

where ρ is the particle density, α the particle volume fraction, \mathbf{u} the particle velocity vector, \mathbf{u}_a the air velocity vector, \mathbf{F} the external force other than drag acting on the particle, and K the air-particle momentum exchange coefficient. When the particle is a water droplet, K is defined according to

$$K = \frac{18\mu f}{\rho d_d^2} \quad (6)$$

where d_d is the droplet diameter, and f the drag function and calculated as

$$f = \frac{C_{\text{DDrop}} Re_p}{24} \quad (7)$$

$$C_{\text{DDrop}} = \begin{cases} 24(1 + 0.15Re_p^{0.687})/Re_p & Re_p \leq 1000 \\ 0.44 & Re_p > 1000 \end{cases} \quad (8)$$

$$Re_p = \frac{\rho_a |\mathbf{u}_a - \mathbf{u}| d_p}{\mu} \quad (9)$$

where C_{DDrop} is the droplet drag coefficient, Re_p the

relative Reynolds number, and d_p the droplet diameter or ice crystal equivalent diameter.

When the particle is an ice crystal, K is defined by

$$K = \frac{3\mu C_{\text{DIce}} Re_p}{4\rho d_i^2} \quad (10)$$

where d_i is the ice crystal equivalent diameter, which is the diameter of a sphere with the same volume as the ice crystal particle. C_{DIce} is the ice crystal drag coefficient.

The equations for local water droplet collection efficiency and local ice crystal collection efficiency are

$$\beta_{\text{drop}} = \frac{\alpha_{\text{drop}} (\mathbf{u}_{\text{drop}} \cdot \mathbf{n})}{\alpha_{\infty, \text{drop}} |\mathbf{u}_{\infty, \text{drop}}|} \quad (11)$$

$$\beta_{\text{ice}} = \frac{\alpha_{\text{ice}} (\mathbf{u}_{\text{ice}} \cdot \mathbf{n})}{\alpha_{\infty, \text{ice}} |\mathbf{u}_{\infty, \text{ice}}|} \quad (12)$$

where α_{drop} and $\alpha_{\infty, \text{drop}}$ are the local water droplet volume fraction near the wall and the water droplet volume fraction in the far field, α_{ice} and $\alpha_{\infty, \text{ice}}$ the local ice crystal volume fraction near the wall and the free flow ice crystal volume fraction, \mathbf{u}_{drop} and \mathbf{u}_{ice} the local water droplet velocity vector and the local ice crystal velocity vector, and $\mathbf{u}_{\infty, \text{drop}}$ and $\mathbf{u}_{\infty, \text{ice}}$ the velocity vector of water droplets and the velocity vector of ice crystals in the free flow. \mathbf{n} is the normal unit vector at the wall.

1.2 Drag coefficient and adhesion model of ice crystals

1.2.1 Drag coefficient model

The shape of ice crystals is affected by the atmospheric environment and altitude, resulting in different shapes and sizes of ice crystals at high altitudes. The shape of ice crystals is diverse, leading to notable discrepancies in air drag between ice crystals and supercooled water droplets in motion. These variations in air drag affect the motion and impingement of the ice crystals on the surface of the aircraft. Therefore, it is necessary to utilize a drag model that takes into consideration the shape of ice crystals. Typically, irregular ice crystals are described in terms of their sphericity Φ .

Particles with different sphericity possess distinct windward areas as they move, thereby generat-

ing diverse airflow drag forces. It is shown that the drag coefficient model proposed by Ganser^[19] has high accuracy in simulating the drag of irregular particles. The formula is as follows

$$C_{D_{ice}} = \frac{24}{Re_p K_1} (1 + 0.1118 (Re_p K_1 K_2)^{0.6567}) + \frac{0.4305 K_2}{1 + \frac{3305}{Re_p K_1 K_2}} \quad (13)$$

where $K_1 = \left(\frac{1}{3} + \frac{2}{3} \Phi^{-1/2}\right)^{-1}$ is the Stokes shape factor and $K_2 = 10^{1.8148(-\lg \Phi)^{0.5743}}$ the Newton shape factor, both related to the particle sphericity.

1.2.2 Adhesion model

Supercooled water is widely believed to adhere to surfaces upon impact, while ice crystals exhibit significant differences. Due to differences in ice crystal size, speed, and the presence of liquid water, the ice crystals may bounce, break, or adhere when they impact a surface^[20-21]. Therefore, it is necessary to introduce an adhesion model for the problem of ice crystal impact adhesion.

Trontin et al.^[22] developed an empirical formula by statistical laws from the NRC experiment records on partially melted ice crystal icing and the NASA-NRC experiment records on mixed-phase icing. The model uses the average melt ratio of ice crystals, total liquid water content, and total ice water content to describe the ice crystal adhesion effect. The ice crystals in this paper did not undergo melting at the initial moment, and any melting that occurred during its movement process is not considered in the calculations due to the minus ambient temperature. Thus, a simplified adhesion model is utilized. The equation is expressed as

$$\epsilon_{s,d} = K_d (Y_d + \eta_{ice} Y_{ice}) \quad (14)$$

where $\epsilon_{s,d}$ is the adhesion efficiency, η_{ice} the melt ratio of ice crystal which equals to 0 in mixed-phase conditions, Y_d the ratio of the mass of supercooled water droplets impinging upon the surface to the total mass impinging upon the surface, and Y_{ice} the ratio of the mass of ice crystals impinging upon the surface to the total mass impinging upon the surface. The sum of Y_d and Y_{ice} is 1. K_d is constant. Y_d and Y_{ice} are expressed as

$$Y_d = \frac{\dot{m}_{c,d}}{\dot{m}_{c,d} + \dot{m}_{c,ice}} \quad (15)$$

$$Y_{ice} = \frac{\dot{m}_{c,ice}}{\dot{m}_{c,d} + \dot{m}_{c,ice}} \quad (16)$$

where $\dot{m}_{c,d}$ is the mass flow rates of water droplets that reach the surface, and $\dot{m}_{c,ice}$ the mass flow rates of ice crystals that reach the surface. The constant in the adhesion model is directly correlated with the surface temperature. If the surface temperature was below the melting point of ice, ice crystals will not adhere. K_d is expressed as

$$K_d = \begin{cases} 0.6 & T_s \geq T_m \\ 0 & T_s < T_m \end{cases} \quad (17)$$

After taking into account the adhesive effect of ice crystals, the true mass flow rate of ice crystals that adhere to the icing surface and participate in the icing process is

$$\dot{m}_{c,ic,i} = \epsilon_{s,d} \cdot U_{\infty,ic} LWC (1 - \eta_{ice}) \beta_{ic} A \quad (18)$$

where $U_{\infty,ic}$ is the velocity of the ice crystal in the far field, liquid water content (LWC) the ice crystal content in the air flow field, β_{ic} the local ice crystal collection efficiency, and A the bottom area of the control volume.

1.3 Icing thermodynamic model in mixed-phase conditions

The icing thermodynamic model for mixed-phase conditions has been expanded based on the Messinger's theory. Heat conduction within the ice layer is disregarded. The control volume method is employed to analyze the processes of mass and energy transfer in the liquid water control volume at the wall.

A schematic of the mass transfer process is shown in Fig.1. The mass flow rates include the mass flow rate of the melted segments of ice crystals impacting the surface $\dot{m}_{c,ic,w}$, the mass flow rate of the not melted segments of ice crystals impacting the surface $\dot{m}_{c,ic,i}$, the mass flow rate of water droplets that reach the surface $\dot{m}_{c,d}$, the inflow/outflow mass flow rate of the control volume \dot{m}_{in} and \dot{m}_{out} , the mass flow rate of evaporation \dot{m}_{ev} , the mass flow rate of water frozen to ice \dot{m}_f , and the mass flow rate of sublimation of ice \dot{m}_{sub} . Thus, the mass conservation equation is expressed as

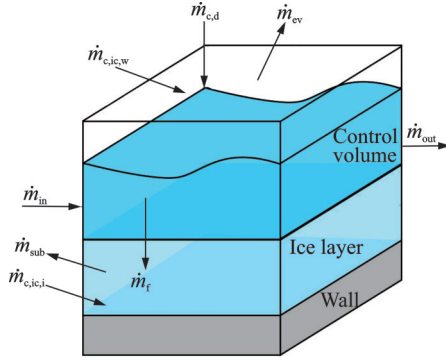


Fig.1 Mass balance of control volume

$$\dot{m}_{c,ic,w} + \dot{m}_{c,d} + \dot{m}_{in} = \dot{m}_f + \dot{m}_{ev} + \dot{m}_{out} \quad (19)$$

The mass flow rate of ice accretion \dot{m}_i is calculated as

$$\dot{m}_i = \dot{m}_{c,ic,i} + \dot{m}_f - \dot{m}_{sub} \quad (20)$$

The energy transfer process involved in the control volume is schematically illustrated in Fig.2. The heat fluxes entering the control volume include the kinetic energy of ice crystals $\dot{Q}_{ke,ic}$, the kinetic energy of supercooled water droplets $\dot{Q}_{ke,d}$, the latent heat of water freezing \dot{Q}_f , the heat conduction due to the temperature difference between the wall temperature and the melting temperature \dot{Q}_{cond} , and the sensible heat of water from the previous control volume \dot{Q}_{in} . The heat fluxes leaving the control volume include the convective heat exchange \dot{Q}_{conv} , the latent heat of water evaporation on the surface \dot{Q}_{ev} or the latent heat of ice sublimation when applicable \dot{Q}_{sub} , the sensible heat of water droplets $\dot{Q}_{c,d}$, the sensible heat of melted part of ice crystals $\dot{Q}_{c,ic,w}$, the sensible heat of un-melted part of ice crystals $\dot{Q}_{c,ic,i}$, and the sensible heat of water exiting the control volume \dot{Q}_{out} . The energy conservation equation is expressed as

$$\dot{Q}_{ke,d} + \dot{Q}_{ke,ic} + \dot{Q}_f + \dot{Q}_{cond} + \dot{Q}_{in} = \dot{Q}_{conv} + \dot{Q}_{ev} + \dot{Q}_{c,d} + \dot{Q}_{c,ic,w} + \dot{Q}_{c,ic,i} + \dot{Q}_{out} \quad (21)$$

In the energy conservation equation and the mass conservation equation, there are corresponding formulas for the calculation of each mass flow rate and heat flux. Please refer to Ref.[17] written by authors for details due to limitations in the length of this paper. By solving the icing thermodynamic model, the surface temperature, runback water, adhesion characteristics of ice crystals, and the ice accretion rate can be obtained.

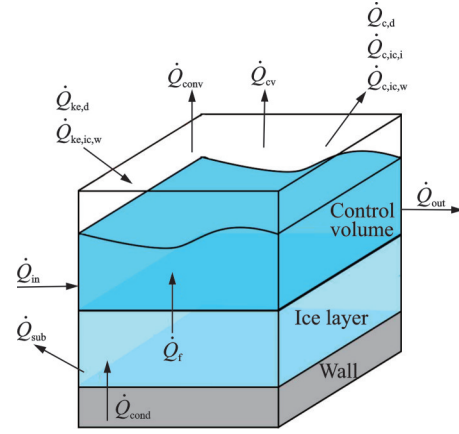


Fig.2 Energy balance of control volume

2 Calculation Methods

2.1 Calculation process

The calculation procedure is illustrated in Fig.3. The simulation is based on the FLUENT software and its user-defined functions (UDFs) programmed by the C Language. Airflow field is calculated and then the water droplets and ice crystals motion are calculated by one-way coupling method using the Eulerian method. Then using the single-step method, the ice crystal adhesion model and icing thermodynamic model are calculated to obtain the ice accretion rate, in which the influence of ice accretion on the air flow field and particle motion is not considered.

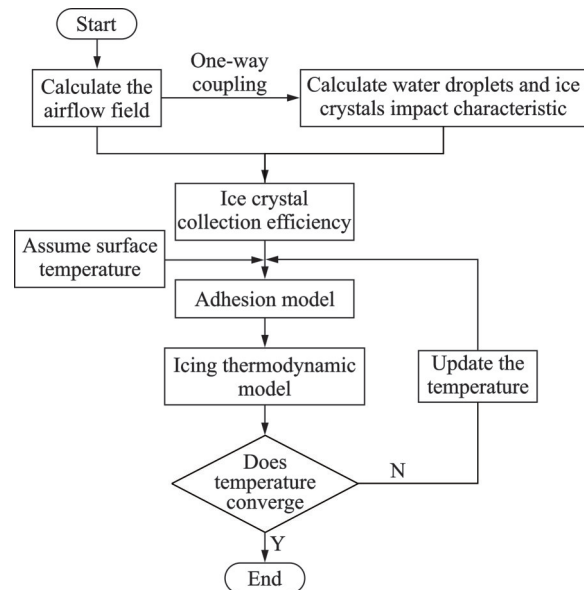


Fig.3 Calculation flowchart

A detailed introduction is as follows.

(1) Calculation of airflow field. The airflow field is calculated by the pressure-based solver with

the Spalart-Allmaras turbulence model selected. Air is treated as the ideal gas. The pressure-far-field and isothermal/adiabatic wall boundary are applied. In order to simulate the effect of roughness due to ice accretion on convective heat transfer, the roughness height on the icing surface is set to be 1mm based on equivalent sand-grain roughness height model. Velocity-pressure coupling is performed using the SIMPLEC algorithm. The standard scheme is used for the discretization of pressure. The second-order upwind scheme is used for other parameters including energy, momentum, and density. The results of air pressure, velocity, heat flux and air shear force on the wall are obtained and exported for subsequent calculations.

(2) Calculation of particle motion. The Eulerian method is utilized to solve governing equations based on the airflow field results. Four user-defined scalars (UDSs) are defined including the particle volume fraction and the velocity in three directions. The second-order upwind scheme^[23] is used for the uds parameters. The local collection efficiencies of water droplets and ice crystals are obtained and exported for subsequent calculations.

(3) Calculation of the adhesion model and icing thermodynamic model. An initial surface temperature is assumed to determine the adhesion mass of ice crystal. The icing thermodynamic model is solved from the stagnation points to downstream control volumes until all surface control volumes looped. The control volumes representing the stagnation point are determined by finding adjacent meshes with air shear forces in opposite directions. The detailed loop method of control volumes for the icing thermodynamic model solution is available in Ref.[24] written by authors from the same investigation group for the three-dimensional icing problem. A new surface temperature can be obtained after the above calculation. The iteration for the ice crystal adhesion and ice accretion model is conducted until it reaches convergence when the temperature difference of adjacent two iteration steps is less than 10^{-6} .

Once the solution is complete, information on ice crystal adhesion, surface temperature, runback water and ice accretion rate can be obtained. Final-

ly, the mass of ice accretion and ice shape in the icing period can be determined.

2.2 Equation discretization

The solution of the control equations for the particles motion requires the discretization of the equations and the second-order upwind format is applied as described in the following paragraphs. The solution of adhesion and icing thermodynamic model mentioned in Section 2.1 just need loop all the surface control volumes as a post-processing calculation.

The discrete form of the second-order upwind format of the particle continuity equation is as

$$\frac{\rho(\alpha_p^{n+1} - \alpha_p^n)}{\Delta t} + F + G + H = 0 \quad (22)$$

$$F = \begin{cases} \frac{\rho}{2\Delta x} (3\alpha_p u_p - 4\alpha_w u_w + \alpha_{ww} u_{ww}) & u_p > 0 \\ \frac{\rho}{2\Delta x} (-3\alpha_p u_p + 4\alpha_e u_e - \alpha_{ee} u_{ee}) & u_p < 0 \end{cases}$$

$$G = \begin{cases} \frac{\rho}{2\Delta y} (3\alpha_p v_p - 4\alpha_n v_n + \alpha_{nn} v_{nn}) & v_p > 0 \\ \frac{\rho}{2\Delta y} (-3\alpha_p v_p + 4\alpha_s v_s - \alpha_{ss} v_{ss}) & v_p < 0 \end{cases}$$

$$H = \begin{cases} \frac{\rho}{2\Delta z} (3\alpha_p w_p - 4\alpha_f w_f + \alpha_{ff} w_{ff}) & w_p > 0 \\ \frac{\rho}{2\Delta z} (-3\alpha_p w_p + 4\alpha_b w_b - \alpha_{bb} w_{bb}) & w_p < 0 \end{cases} \quad (23)$$

The discrete form of the momentum equation in the x direction is as follows, and the momentum equations in the y and z directions have the same form.

$$\frac{\rho(\alpha_p^{n+1} u_p^{n+1} - \alpha_p^n u_p^n)}{\Delta t} + I + J + L = \rho \alpha K (u_{a,p} - u_p) \quad (24)$$

$$I = \begin{cases} \frac{\rho}{2\Delta x} (3\alpha_p u_p u_p - 4\alpha_w u_w u_w + \alpha_{ww} u_{ww} u_{ww}) & u_p > 0 \\ \frac{\rho}{2\Delta x} (-3\alpha_p u_p u_p + 4\alpha_e u_e u_e - \alpha_{ee} u_{ee} u_{ee}) & u_p < 0 \end{cases}$$

$$J = \begin{cases} \frac{\rho}{2\Delta y} (3\alpha_p u_p v_p - 4\alpha_n u_n v_n + \alpha_{nn} u_{nn} v_{nn}) & v_p > 0 \\ \frac{\rho}{2\Delta y} (-3\alpha_p u_p v_p + 4\alpha_s u_s v_s - \alpha_{ss} u_{ss} v_{ss}) & v_p < 0 \end{cases}$$

$$L = \begin{cases} \frac{\rho}{2\Delta z} (3\alpha_p u_p w_p - 4\alpha_f u_f w_f + \alpha_{ff} u_{ff} w_{ff}) & w_p > 0 \\ \frac{\rho}{2\Delta z} (-3\alpha_p u_p w_p + 4\alpha_b u_b w_b - \alpha_{bb} u_{bb} w_{bb}) & w_p < 0 \end{cases} \quad (25)$$

where u , v and w denote the velocity components of the fluid in the x , y , and z directions individually. Δt and Δx , Δy , Δz denote the discretization step in time and space, respectively. The subscripts p , w , n , etc. represent the location of the grid points of the control volume as shown in Fig.4.

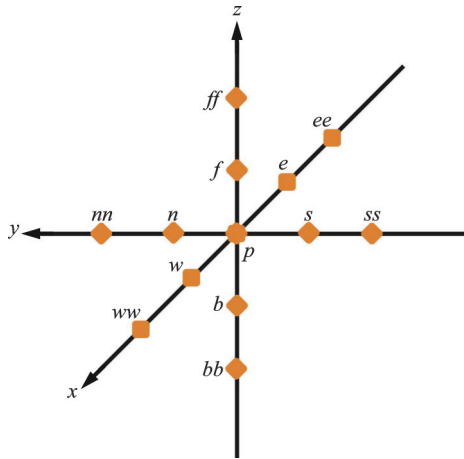


Fig.4 Position relationship of control volume

3 Validation of Adhesion and Icing Thermodynamic Model

The mixed-phase icing experiments carried out by Al-Khalil in the Cox Ice Wind Tunnel (IWT) are used for validation^[25]. A NACA-0012 airfoil with a chord length of 0.911 4 m was used in Al-Khalil's experiment. The experimental conditions are shown in Table 1, where AoA represents the angle of attack, and MVD represents the mean volume diameter.

Table 1 Calculation conditions for icing

Parameter	Value
Altitude/km	0.25
Pressure/Pa	98 000
Temperature/K	260.65
Ma	0.165
LWC/(g·m ⁻³)	0.7
MVD of water drops / μm	20
IWC/(g·m ⁻³)	0.3
MVD of ice crystals / μm	150
AoA/(°)	0
Icing time/s	600

The grid is shown in Fig.5. The total number of the grid is 288 091. The calculation zone radius is 10 m which satisfies the far-pressure boundary conditions. Grid-independent verification is performed with the bottom grid height of 0.1, 0.05, and 0.005 mm, and the different grids have the same grid points, with the same growth ratio of 1.1. The drag and lift coefficients, the heat transfer intensity represented by Frossling number defined as $Fr = hL/\lambda Re^{1/2}$ are calculated and compared for different grids. The relative errors of the drag and lift coefficients for the meshes with 0.005 and 0.05 mm bottom grid height are within 0.5%, and the relative error of Fr for the same meshes is within 1%. In the definition of Fr , h is the convective heat transfer coefficient, L the characteristic length, and λ the thermal conductivity of air.

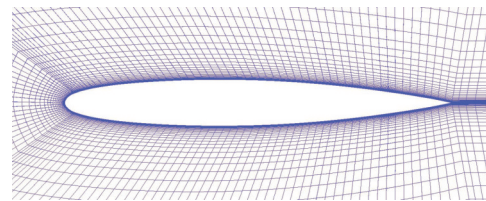


Fig.5 NACA-0012 mesh

In summary, the grid with a bottom grid height of 0.05 mm is chosen for flow field and heat transfer calculations. Meanwhile, the y^+ values along the airfoil surface are all less than 1.

Fig.6 shows the comparison between the simulation results of ice accretion with the experimental results. The results show that the limits of ice accretion between simulations and experiments are relatively congruent. Consequently, the models in this paper can be applied to simulate the icing process under mixed phase conditions.

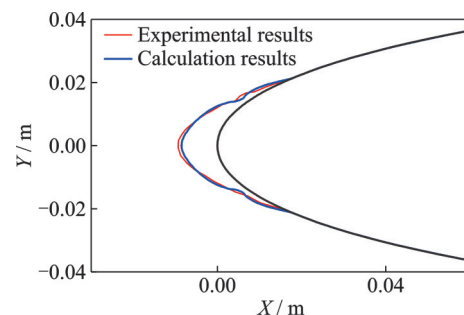


Fig.6 Ice shape of simulations and experiments

4 Calculation Results and Analysis of Multi-element Airfoil

4.1 Calculation object and conditions

A three-dimensional multi-element airfoil structure with a chord length of 1.2 m, as shown in Fig.7, is investigated in this paper. The icing conditions of eight cases(Cases 1—8)are shown in Table 2. Cases 1—4 are the icing conditions in the Cox IWT experiments^[25] and Cases 5—8 are the mixed-phase icing conditions given in Appendix D of FAR 33^[26]. To reduce the number of independent variables for different calculation conditions, the sphericity for calculation conditions in Table 2 is 1. The influence of sphericity is discussed in Section

4.4. Case 1 and Case 2 have the same ambient temperature which is higher than that of Case 3 and Case 4. Case 1 is the supercooled water condition while Case 2 is the mixed-phase condition. Case 3 and Case 4 have different liquid water and ice crystal contents. Cases 5—8 have the same average droplet and ice crystal diameter but have differences in ambient pressure, temperature, flight speed, liquid water content, and flight angle of attack.



Fig.7 Geometry model of multi-element airfoil

Table 2 Calculation conditions for icing of Cases 1—8

Parameter	Case 1	Case 2	Case 3	Case 4	Case 5	Case 6	Case 7	Case 8
Altitude/km	0.25	0.25	0.25	0.25	1.0	1.5	3.0	3.0
Pressure/Pa	98 000	98 000	98 000	98 000	89 867	84 545	70 089	70 089
Temperature/K	266.15	266.15	260.65	260.65	268.15	263.15	263.15	253.15
Ma	0.163	0.163	0.165	0.165	0.405	0.360	0.449	0.445
LWC/(g·m ⁻³)	0.7	0.7	0.3	0.7	0.55	0.43	0.43	0.2
MVD of water drops/μm	20	20	20	20	20	20	20	20
IWC/(g·m ⁻³)	0	0.7	0.7	0.3	0.45	0.57	1.87	1.5
MVD of ice crystals/μm	—	200	150	150	150	150	150	150
$AoA/(^{\circ})$	0	0	0	0	4	2.2	1	1
Ice time/s	600	600	600	600	600	600	600	600

4.2 Mesh independence verification

The computational domain for the multi-element airfoil has a radius of 10 m to ensure the pressure-far-field boundary and its mesh is a structured mesh with 2.16 million grids, as shown in Fig.8.

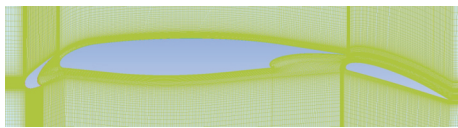


Fig.8 2D section mesh of multi-element airfoil

Grid-independent verification is performed using the bottom mesh height of 1.000, 0.250, 0.050, and 0.025 mm, and the grid points of all grids are the same, with the same growth ratio of 1.1. The grid independence verification is confirmed by comparing the pressure coefficient, the drag and lift coefficients, and the Fr number with different grids.

Taking Case 2 as an example, the pressure coefficient results are presented in Fig.9, where X/C is the ratio of the airfoil horizontal coordinate to the chord length. It is shown that the bottom grid height has little effect on the pressure coefficient, there are small wavy in the pressure coefficient of the main wing, possibly caused by the insufficient precision in the geometry used. The relative errors of the drag and lift coefficients are shown in Table 3, which are based on the results of the grid with 0.025 mm bottom grid height. It is shown that the relative error in lift and drag coefficients of the 0.050 mm bottom grid height is less than 0.1%. The Fr numbers of these meshes are shown in Fig.10, where $S=0$ is the geometry stagnation point of the multi-element airfoil. It is calculated that the relative error in Fr number between the grids of 0.050 and 0.025 mm bottom grid height is less than 1%.

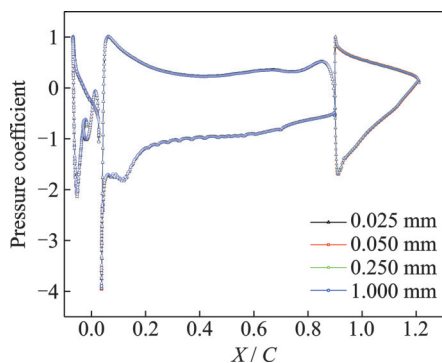
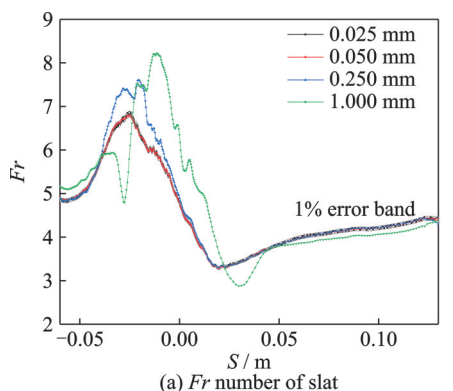


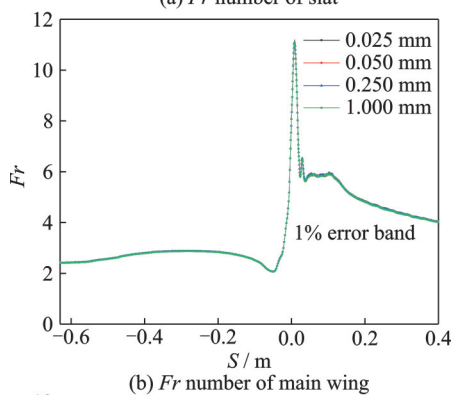
Fig.9 Pressure coefficient

Table 3 Relative errors of lift and drag coefficients

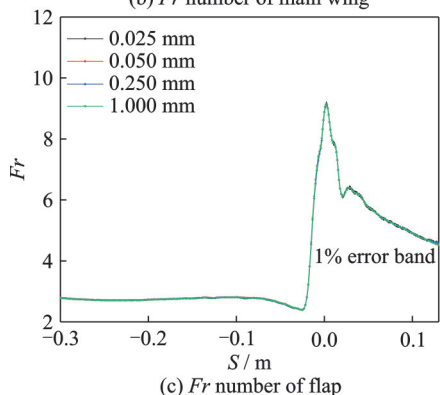
y_p /mm	0.025	0.050	0.250	1.000
Lift coefficient	0.559 7	0.559 8	0.559 9	0.559 4
Relative error/%		0.00	0.04	0.06
Drag coefficient	0.013 44	0.013 43	0.013 41	0.013 34
Relative error/%		0.07	0.22	0.75



(a) Fr number of slat



(b) Fr number of main wing



(c) Fr number of flap

Fig.10 Fr numbers for grids with different bottom grid height

In summary, the grid with a bottom mesh height of 0.05 mm ($y^+ < 1$ in all bottom grids along the airfoil surface) is chosen for the flow field and heat transfer calculations.

4.3 Airflow field results

The velocity contours are similar for Cases 1—4 because of nearly the same inlet velocity and the same AoA. The airflow fields are significantly different for Cases 5—8 owing to different AoA and inlet velocity. Taking Case 2 as an example, Fig.11 presents the streamline diagram of the airflow field. It is observed that the airflow field is complicated and vortices are visible at the back of both the slat and the main wing. The air flow passes through the gaps between the slat and main wing, the main wing and flap, arriving at the upper surface of the wing.

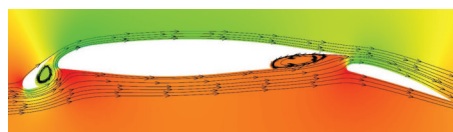


Fig.11 Streamline diagram of Case 2

By comparing the temperature distribution results, it is found that the temperature contours for Cases 5—8 are very different with Cases 1—4 because of the higher velocity and AoA. For example, Fig.12 and Fig.13 show the temperature contours of Case 2 and Case 5, respectively. It is seen that there is relative high temperature in Case 5 near the wall where is backward of wind near the vortices. By analyzing the temperature contours of all cases, it is found that there is only the Case 5 in which the maximum temperature of the air exceeds the melt temperature. Because the high temperature region is small, there is a small amount of heat exchange between the ice crystals and the air. It is believed that the amount of heat is insufficient to cause the ice crystals to begin melting.

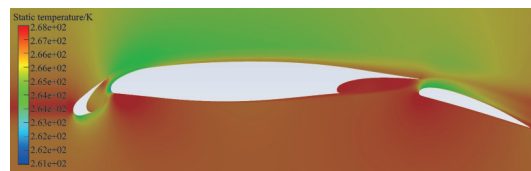


Fig.12 Temperature contours of Case 2



Fig.13 Temperature contours of Case 5

4.4 Analysis of impingement characteristics results

The contours of water and ice crystal collection efficiency of Case 2 are shown in Fig.14 and Fig.15 individually. The impingement zone of water droplets in Case 2 is mainly concentrated on the leading edge of the slat and flap, and there are few impingement droplets on main wing due to the shelter effect. While the impingement zone of ice crystals in Case 2 is quite larger than that of water droplets especially on the upper surface of the slat and the lower surface of the flap. It is because that ice crystals are larger and possess higher inertial force than water droplets. The enlarged contours of the water droplets and ice crystals collection efficiency for the slat and flap are shown in Fig.16.

2D plots of water droplets and ice crystals collection efficiency for the eight cases on the slat, main wing and the flap are shown in Figs.17—19. It is seen from Figs.17, 19 that the peak values of the collection efficiency of water droplets and ice crystals are around the geometry stagnation point of the slat and flap. Ice crystals have a higher collection ef-

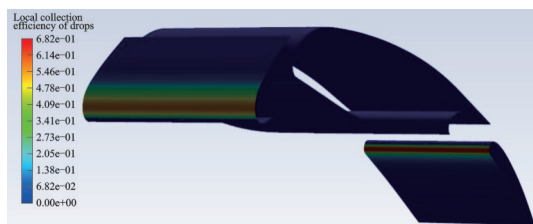


Fig.14 Contours of water droplets collection efficiency of Case 2

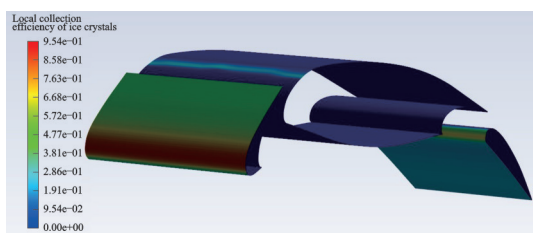
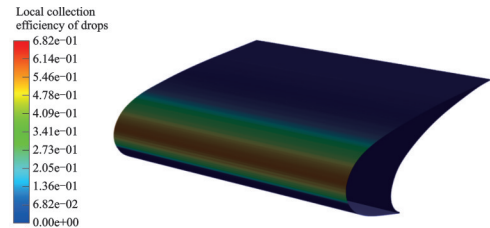
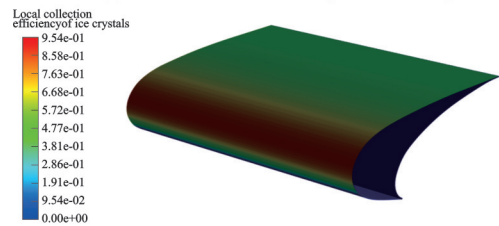


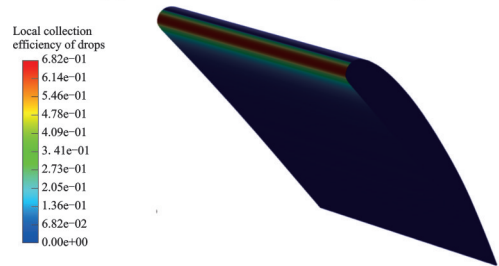
Fig.15 Contours of ice crystals collection efficiency of Case 2



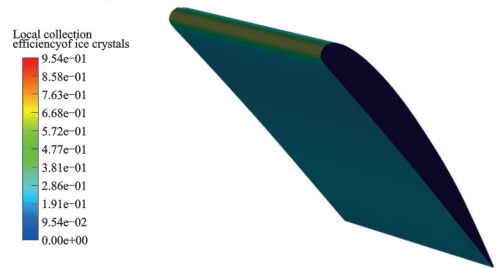
(a) Slat collection efficiency of water droplets



(b) Slat collection efficiency of ice crystals



(c) Flap collection efficiency of water droplets



(d) Flap collection efficiency of ice crystals

Fig.16 Contours of the collection efficiency for slat and flap

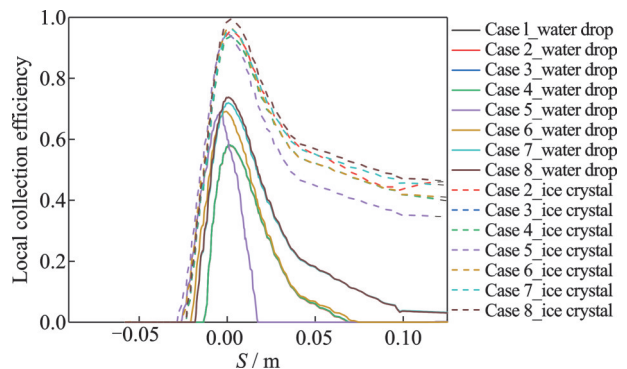


Fig.17 2D plot of water droplets and ice crystal collection efficiency for slat

ficiency compared to water droplets due to their greater inertia. The impingement zone of ice crystals covers the entire windward surface. It should be noted that the angle of attack has great influence on the collection efficiency for main wing due to the

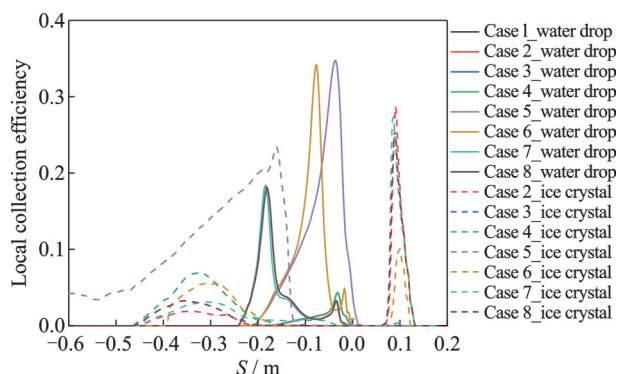


Fig.18 2D plot of water drops and ice crystal collection efficiency for main wing

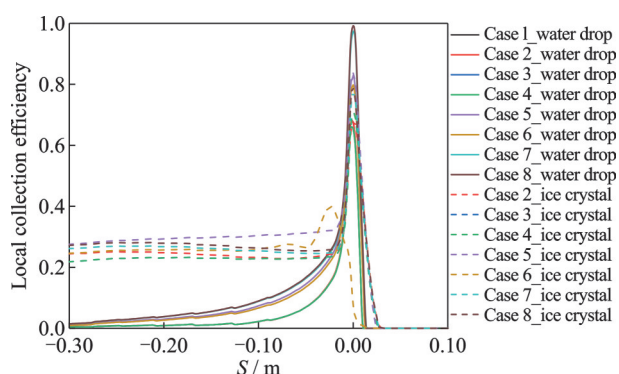


Fig.19 2D plot of water drops and ice crystal collection efficiency for flap

multi-element geometry effects, as shown in Fig.18. In Case 5, a large area of ice crystals formed on the lower surface of the main wing. Therefore, changes in angle of attack and flight speed can cause significant variation in the impingement characteristics.

As shown in Fig.18, it seems that the impingement area of the water droplets is concentrated on the lower surface, with a small impact zone. Except for the cases with large angles of attack (Case 5 and Case 6), the maximum local water droplet collection efficiency on main wing in other cases is less than 0.2. For small AoA, ice crystals impact the upper surface and form an impact zone. The impingement characteristics of ice crystals on the lower surface are similar to those of water droplets, the impingement limit will be closer to the rear of the main wing. Although the impingement area of the water droplets is smaller than that of ice crystals, in the case of relative high temperature or high LWC, the impingement water will not completely freeze and

will continue flow backwards, producing a larger runback water zone. The ice crystals impact on the runback water zone may produce additional adhesion. As a result, the mixed phase icing will be more intense during the fully developed stage of the runback water, and the schematic diagram of this condition is shown in Fig.20.

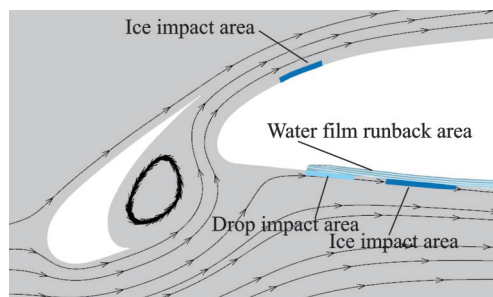


Fig.20 Schematic of additional ice crystals adhesion

Sphericity Φ also influences the impingement characteristics of the ice crystal. The impingement characteristics are calculated for different sphericity values (1.0, 0.8, and 0.6) based on the specified conditions in Case 2. The results are shown in Figs.21—23. Different sphericity would produce large differences of collection efficiency on the main wing. The slat and flap have comparable impingement characteristics, and the ice crystal collection efficiency increases slightly as the ice crystal shape approaches spherical. Overall, the sphericity of ice crystals affects the collection efficiency on the slat and flap and the impact location on the main wing. For the entire wing, sphericity has small effect on the impingement characteristics.

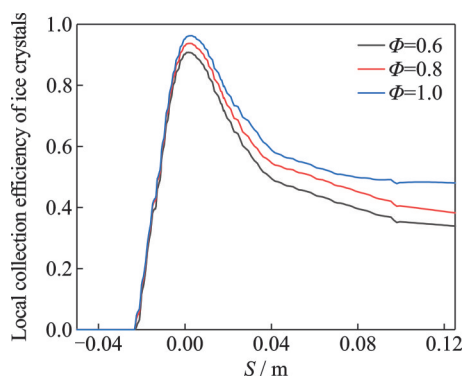


Fig.21 Influence of ice crystal sphericity on collection efficiency for slat (Case 2)

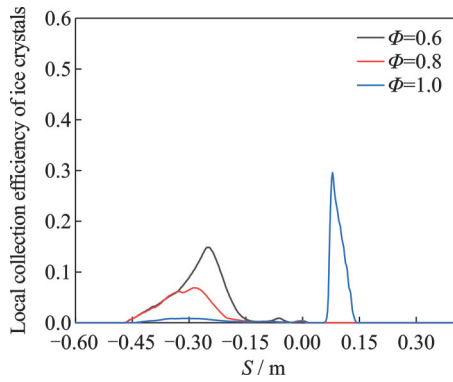


Fig.22 Influence of ice crystal sphericity on collection efficiency for main wing (Case 2)

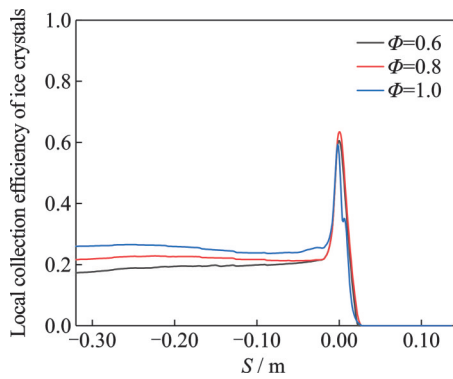


Fig.23 Influence of ice crystal sphericity on collection efficiency for flat (Case 2)

It has been found from the previous calculations that changes in AoA affect the airflow field and also have a great impact on the collection efficiency of water droplets and ice crystals. To illustrate for detail, AoA is changed under the calculation condition in Case 2. The collection efficiencies for water droplets and ice crystals are calculated at AoA of 0°, 2°, and 5°, respectively. The results are shown in Figs.24—26. It can be found that for the slat and flap, the variation in the flight angle of attack primarily affects the stagnation point position and peak collection efficiency. For the main wing, the changes in flight AoA have significant impacts, where the ice crystal impact zone extends to the entire lower surface when the AoA is 5°. It should also be noted that the maximum value of the water droplet collection efficiency reaches a maximum value of 1.7 on the main wing when AoA is large. The reason is that the airflow passes through the gap between the slat and the main wing, while the water droplets cannot pass through the gap.

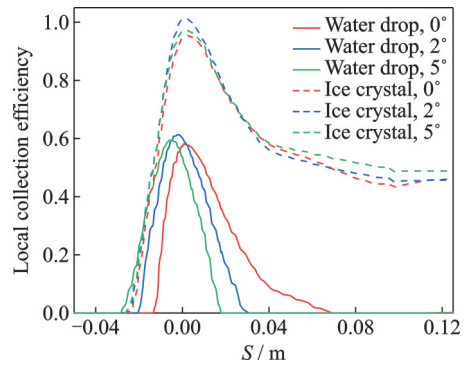


Fig.24 Influence of AoA on collection efficiency for slat

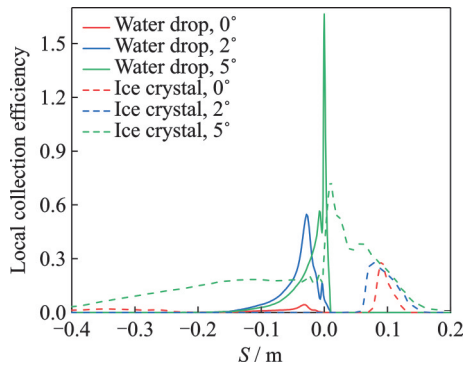


Fig.25 Influence of AoA on collection efficiency for main wing

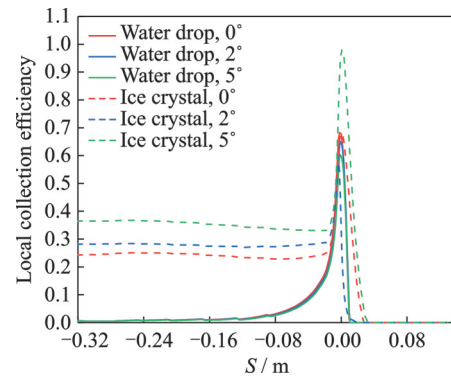


Fig.26 Influence of AoA on collection efficiency for flap

Therefore, the changes in AoA have a great influence on the impingement characteristics of the multi-element airfoil. This feature must be taken into account in anti-icing design.

4.5 Analysis of adhesion characteristics and icing results

The adhesion efficiency, adhesion mass flow rate of ice crystals and ice accretion rate can be attained through the resolution of the adhesion and icing thermodynamic model. The results of the adhesion efficiency and adhesion mass of the ice crystals

for Cases 2—8 are displayed in Figs.27—29. It has been found that ice crystals exhibit strong adhesion in the impingement zone of water droplets, resulting in a large number of ice crystals adhering to the ar-

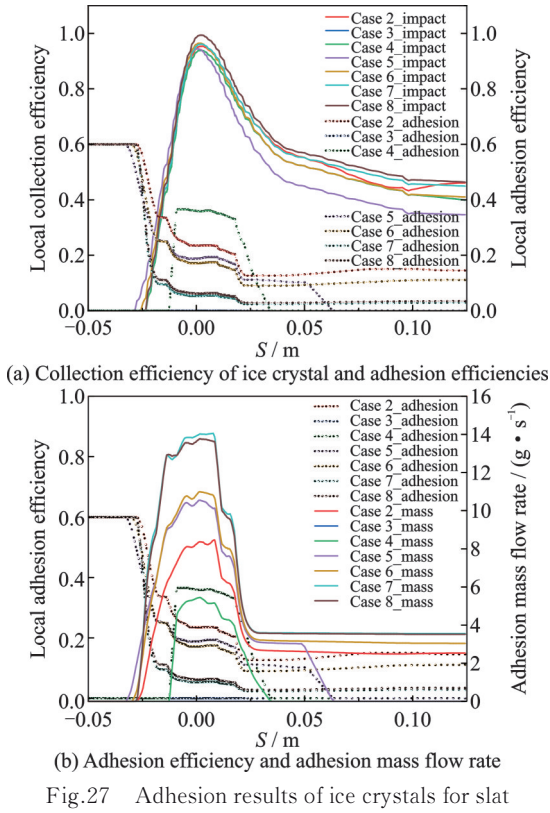


Fig.27 Adhesion results of ice crystals for slat

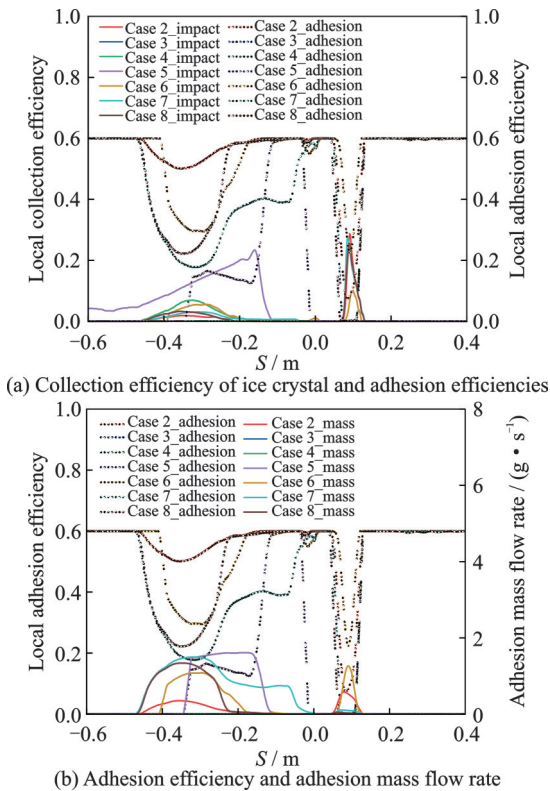
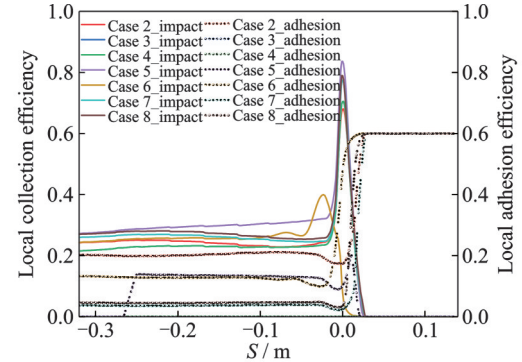
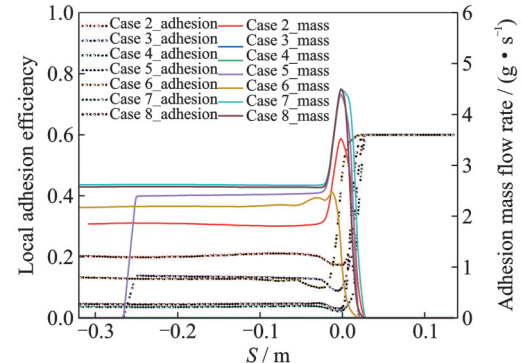


Fig.28 Adhesion results of ice crystals for main wing



(a) Collection efficiency of ice crystal and adhesion efficiencies



(b) Adhesion efficiency and adhesion mass flow rate

Fig.29 Adhesion results of ice crystals for flap

ea. In glaze ice conditions, the impact water will not fully freeze and form a runback water film. Ice crystal will adhere the water runback zone when it impacts this zone, as can be seen in Cases 2—6. In the area where no ice crystals impact, the adhesion efficiency is relatively high, with a value of 0.6, due to the existence of liquid water, as determined by the adhesion model algorithm. However, since the absence of ice crystals, there will be no adhesion of ice crystals in this zone.

Differences in LWC can alter icing conditions and subsequently affect the adhesion of ice crystals. When comparing Case 3 and Case 4 with the same conditions but different levels of liquid water content, the results show that the liquid water in Case 3 freezes entirely, resulting in zero adhesion efficiency and no adhesion of ice crystals. To further clarify this issue, the adhesion efficiencies of ice crystals for four LWCs (0.3, 0.5, 0.7, and 1.0 g/m³) are calculated under the same conditions as in Case 4. Fig.30 illustrates the influence of LWC on the adhesion efficiency of ice crystals for the slat. It is shown that there is no adhesion appeared in the entire region in the case with LWC of 0.3 g/m³. As the

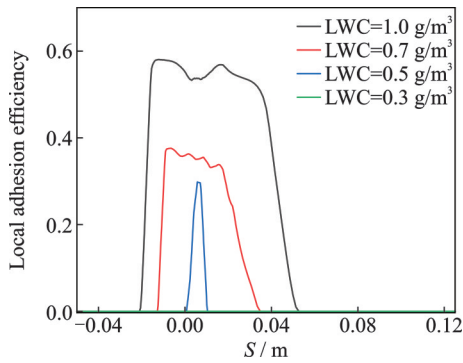


Fig.30 Influence of LWC on adhesion efficiency of ice crystals for slat

LWC increases, both the adhesion efficiency and the adhesion zone gradually expand.

The adhesion characteristics of the slat and flap are similar. The water droplets impingement zone has a relatively high adhesion efficiency, where ice crystals primarily adhere. When with high LWC, the runback water zone becomes larger, causing the adhesion area to expand to the entire impact surface. The slat has more adhesion mass compared to the flap. Therefore, the design of anti/de-icing for mixed phase icing should focus on the slat for large LWC situations.

For the main wing, due to the slat shield effect and the gap between the slat and the main wing, resulting the airflow complex, the amount of ice crystal adhesion is very small, and the ice crystal adhesion zone is mainly concentrated on the lower surface.

Fig.31 illustrates the shapes of ice accretion under mixed phase conditions. The results show that icing primarily accumulated on the slat and flap. In Case 5, significant ice accretion appears on the lower surface of the main wing due to the high angle of attack. Additionally, ice crystals impact the runback water zone on the slat and flap, resulting in ice accretion on the entire surface. These findings are consistent with the adhesion results in the previous section.

Based on the analysis, it is found that mixed phase icing conditions can aggravate the ice accretion of multi-element airfoil and may cause more serious flight hazards.

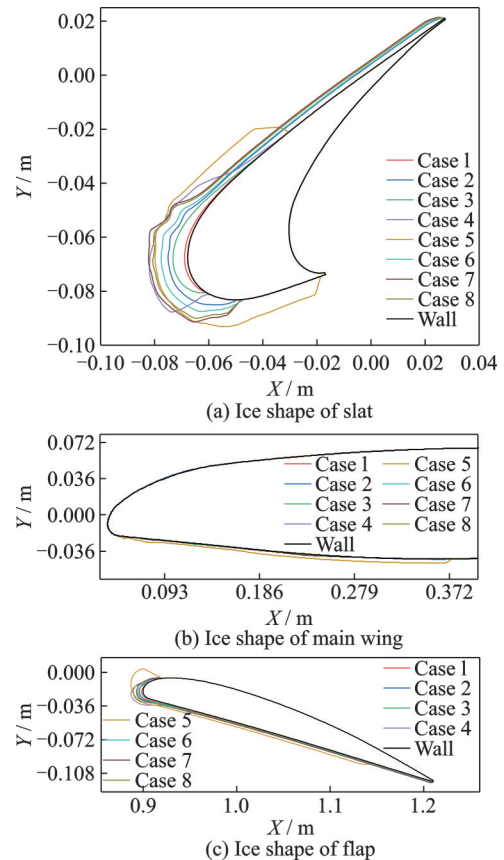


Fig.31 Ice shapes under different conditions

5 Conclusions

Adhesion and icing thermodynamic models are applied and validated. Icing calculations are carried out for a quasi-three-dimensional multi-element airfoil. The impingement and adhesion characteristics of ice crystals and ice accretion on multi-element airfoil are analyzed under different mixed-phase conditions.

(1) The geometry of the multi-element airfoil is complex, it is found that the impingement characteristics of ice crystals are most affected by the flight angle of attack among various flight parameters.

(2) The adhesion effect of ice crystals must be considered under mixed phase conditions.

(3) Ice crystals will adhere to the runback water zone outside the water droplets impingement zone, which may be one of the key considerations for anti/de-icing design under mixed phase conditions.

(4) An increase in LWC/TWC significantly increases the ice crystal adhesion efficiency and adhesion mass flow rate.

References

- [1] TRAN P, BRAHIMI M T, PARASCHIVOIU, et al. Ice accretion on aircraft wings with thermodynamic effects[J]. *Journal of Aircraft*, 1995, 32(2): 444-446.
- [2] OZGEN S, CAMBEK M. Ice accretion simulation on multi-element airfoils using extended Messinger model[J]. *Heat Mass Transfer*, 2009, 45: 305-322.
- [3] NILAMDEEN S, HABASHI W, MARTIN A, et al. FENSAP-ICE: Modeling of water droplets and ice crystals: AIAA-2009-4128[R]. Reston: AIAA, 2009.
- [4] MASON I G, STRAPP J W, CHOW P. The ice particle threat to engines in flight: AIAA-2006-206[R]. Reston: AIAA, 2006.
- [5] MASON I G, CHOW P, FULEKI D M. Understanding ice crystal accretion and shedding phenomenon in jet engines using a rig test[J]. *Journal of Engineering for Gas Turbines and Power*, 2011, 133(4): 041201.
- [6] OLIVER M J. Validation ice crystal icing engine test in the propulsion systems laboratory at NASA Glenn Research Center: AIAA-2014-2898[R]. Reston: AIAA, 2014.
- [7] GOODWIN R V, DISCHINGER D G. Turbofan ice crystal rollback investigation and preparations leading to inaugural ice crystal engine test at NASA PSL-3 test facility: AIAA-2014-2895[R]. Reston: AIAA, 2014.
- [8] BAUMERT A, BANSÄER S E, BACHER M. Implementation of an innovative ice crystal generation system to the icing wind tunnel Braunschweig[J]. *Foundations of Systems Biology*, 2013, 175(1/2): 1.
- [9] MANUEL R, CHO Y. Analysis of ice crystal ingestion as a source of ice accretion inside turbofans: AIAA-2008-4165[R]. Reston: AIAA, 2008.
- [10] WRIGHT W, JORGENSON P, VERES J. Mixed phase modeling in GlennICE with application to engine icing: AIAA-2010-7674[R]. Reston: AIAA, 2010.
- [11] HABASHI W G, NILAMDEEN S. Multiphase approach toward simulating ice crystal ingestion in jet engines[J]. *Journal of Propulsion and Power*, 2015, 27(5): 959-969.
- [12] NORED E, VAN DER WEIDE E T A, HOEIJMAKERS H W M. Eulerian method for ice crystal icing[J]. *AIAA Journal*, 2018, 56(1): 222-234.
- [13] NORED E, SENONER J M, VAN DER WEIDE E T A, et al. Eulerian and Lagrangian ice-crystal trajectory simulations in a generic turbofan compressor[J]. *Journal of Propulsion and Power*, 2019, 35(1): 26-41.
- [14] ZHANG L F, LIU Z X, ZHANG M H. Numerical simulation of ice accretion under mixed-phase conditions[J]. *Proceeding of IMechE Part G: Aerospace Engineering*, 2016, 230(13): 2473-2483.
- [15] YUAN Qin hao, FAN Jiang, BAI Guangchen. Review of ice crystal icing in aero-engines[J]. *Journal of Propulsion Technology*, 2018, 39(12): 2641-2650. (in Chinese)
- [16] JIANG Feifei, DONG Wei, ZHENG Mei, et al. Phase change heat transfer characteristic of ice crystal ingested into turbofan engine[J]. *Journal of Aerospace Power*, 2019, 34(3): 567-575. (in Chinese)
- [17] BU Xueqin, LI Hao, HUANG Ping, et al. Numerical simulation of mixed phase icing on two-dimensional airfoil[J]. *Acta Aeronautica et Astronautica Sinica*, 2020, 41(12): 200-210. (in Chinese)
- [18] MA Yijian, CHAI Delin, WANG Qiang, et al. Phase change and adhesion characteristics of ice crystal movements in wing icing[J]. *Acta Aeronautica et Astronautica Sinica*, 2023, 44(1): 41-52. (in Chinese)
- [19] GANSER G H. A rational approach to drag prediction of spherical and nonspherical particles[J]. *Powder Technology*, 1993, 77(2): 143-152.
- [20] HAUK T, BONACCURSO E, ROISMAN I V, et al. Ice crystal impact onto a dry solid wall. Particle fragmentation[J]. *Proceedings of the Royal Society A: Mathematical, Physical and Engineering Sciences*, 2015, 471(2181): 20150399.
- [21] ROISMAN I V, TROPEA C. Impact of a crushing ice particle onto a dry solid wall[J]. *Proceedings of the Royal Society A: Mathematical, Physical and Engineering Sciences*, 2015, 471(2183): 20150525.
- [22] TRONTIN P, BLANCHARD G, VILLEDIEU P. A comprehensive numerical model for mixed-phase and glaciated icing conditions: AIAA-2016-3742[R]. Washington: AIAA, 2016.
- [23] YANG Shenghua, LIN Guiping, SHEN Xiaobin, et al. Water droplet impingement prediction for three-dimensional complex surfaces[J]. *Journal of Aerospace Power*, 2010, 25(2): 284-290. (in Chinese)
- [24] SHEN X B, LUI G P, YU J, et al. Three-dimensional numerical simulation of ice accretion at the engine inlet[J]. *Journal of Aircraft*, 2013, 50(2): 635-642.
- [25] AL-KHALIL K, IRANI E. Mixed-phase icing simulation and testing at the cox icing wind tunnel: AIAA-2003-0903[R]. Reston: AIAA, 2003.
- [26] MAZZAWY R S, STRAPP J W. Appendix D—An interim icing envelope: 2007-01-3311[R]. [S.l.]: SAE, 2007.

Acknowledgements This research was funded by the National Key R&D Program of China (No.2021YFB2601700), the National Natural Science Foundation of China (No. 52272428), the National Science and Technology Major Project of China (No.J2019-III-0010-0054), and the Fundamental Research Funds for the Central Universities (No.YWF-23-SDHK-L-003).

Authors Mr. LIU Zonghui is the doctoral student in School of Aeronautic Science and Engineering, Beihang University, Beijing, China. His research interests include aircraft anti-icing technology and ice crystal icing.

Dr. BU Xueqin received her Ph.D. degree in School of Aeronautic Science and Engineering, Beihang University, Beijing, China, in 2010. Now she is an associate professor in

Beihang University. Her current research interests include aircraft icing and anti-icing problems, design of hot air anti-icing system, 3D surface icing simulation, complex jet flow heat transfer, ice crystal icing, etc.

Author contributions Mr. LIU Zonghui performed the simulation calculations and wrote this manuscript. Dr. BU Xueqin designed the models and revised the manuscript. Dr. HUANG Ping wrote the computational program. Prof. LIN Guiping contributed to the discussion. Mr. WANG Yudong processed some simulation data. All authors commented on the manuscript draft and approved the submission.

Competing interests The authors declare no competing interests.

(Production Editor: SUN Jing)

混合相结冰条件下多段翼的撞击黏附与积冰的数值模拟

刘宗辉¹, 卜雪琴¹, 黄平¹, 林贵平^{2,1}, 王毓栋¹

(1. 北京航空航天大学航空科学与工程学院, 北京 100083, 中国;

2. 北京航空航天大学杭州创新研究院, 杭州 311115, 中国)

摘要:随着飞机结冰问题研究的深入,混合相结冰问题已经成为研究热点。本文使用了阻力模型、黏附模型和结冰热力学模型来计算混合相结冰条件下的准三维多端翼的结冰情况。首先对多段翼进行了网格划分和空气流场计算。然后进行了数值模拟计算,分析了混合相结冰条件下冰晶的撞击、黏附和积冰特征。结果表明,在本研究的条件下,冰晶的黏附质量流量很高,会对飞行安全造成威胁,并且冰晶在溢流水区域也会发生黏附。此外,随着液态水含量(Liquid water content, LWC)与总水含量(Total water content, TWC)比值的升高,冰晶更容易黏附在表面并参与表面结冰。

关键词:多段翼;混合相结冰;撞击模型;黏附模型;结冰热力学模型